Journal of the Mechanics and Physics of Solids 60 (2012) 1462–1477

Contents lists available at SciVerse ScienceDirect

Journal of the Mechanics and Physics of Solids

journal homepage: www.elsevier.com/locate/jmps

A direct comparison of non-destructive techniques for determining bridging stress distributions

R.B. Greene [a], S. Gallops [a], S. Fünfschilling [b,1], T. Fett [b], M.J. Hoffmann [b], J.W. Ager III [c], J.J. Kruzic [a,*]

[a] Materials Science, School of Mechanical, Industrial, and Manufacturing Engineering, Oregon State University, Corvallis, OR, USA
[b] Institute for Ceramics in Mechanical Engineering, Karlsruhe Institute of Technology, D-76131 Karlsruhe, Germany
[c] Materials Sciences Division, Lawrence Berkeley National Laboratory, Berkeley, CA, USA

ARTICLE INFO

Article history:
Received 23 December 2011
Received in revised form
9 April 2012
Accepted 15 April 2012
Available online 25 April 2012

Keywords:
Bridging stress distribution
Fracture mechanisms
Ceramic material
R-curves
T-stress

ABSTRACT

Crack bridging is an important source of crack propagation resistance in many materials and the bridging stress distribution as a function of crack opening displacement is widely believed to represent a true material property uninfluenced by sample geometry, loading conditions, and other extrinsic factors. Accordingly, accurate measurement of the bridging stress distribution is needed and many non-destructive methods have been developed. However, there are many challenges to accurately determining bridging stresses. A comparison of bridging stresses measured using *R*-curve, crack opening displacement (COD), and spectroscopy methods has been made using two bridging ceramics, Y_2O_3 and MgO doped Si_3N_4 and 99.5% pure Al_2O_3. The COD method is surface sensitive and gives a lower peak bridging stress compared to the *R*-curve technique which samples through the entire material thickness. This is attributed to a more compliant near surface bridging zone. Conversely, when *R*-curves rise steeply over the first few micrometers of growth from a notch, an effect of negative *T*-stress is expected to raise the *R*-curve determined peak bridging stress. Spectroscopy methods were only found to yield reliable bridging stress results if a reasonable through thickness volume of material is sampled. It was found that 2.5% of the specimen thickness achieved using fluorescence spectroscopy appears adequate for Al_2O_3 while 0.1–0.2% of the sample thickness achieved using Raman spectroscopy for Si_3N_4 appears inadequate. Overall, it is concluded that in the absence of *T*-stresses a bridging distribution can be determined that is a true material property. Also, a new method is proposed for determining the bridging stresses of fatigue cracks from (1) the bridging stress distribution for monotonically loaded cracks and (2) experimental fatigue data.

1. Introduction

Crack bridging is an important source of crack propagation resistance in many engineering materials including reinforced brittle and ductile matrix composites (Marshall et al., 1985; Nairn et al., 1991), laminated composites (Bloyer et al., 1998), grain bridging monolithic ceramics (Becher, 1991; Bennison and Lawn, 1989), and multi-phase metallic/intermetallic alloys (Campbell et al., 1999; Kruzic et al., 2005b). It is also important in many biological materials such as

* Corresponding author. Tel.: +1 541 737 7027; fax: +1 541 737 2600.
E-mail address: jamie.kruzic@oregonstate.edu (J.J. Kruzic).
[1] Present address: sia Abrasives Industries AG, Frauenfeld, Switzerland.

0022-5096/$ - see front matter © 2012 Elsevier Ltd. All rights reserved.
http://dx.doi.org/10.1016/j.jmps.2012.04.007

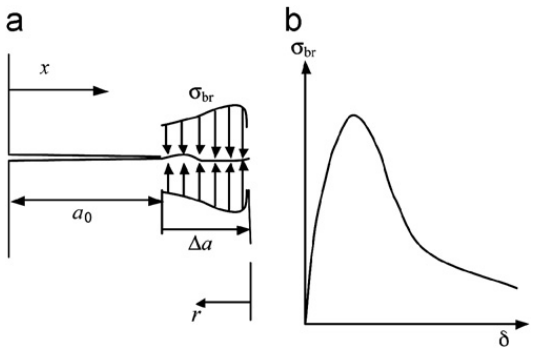

Fig. 1. (a) Schematic representation of a crack in a material exhibiting crack surface interactions by bridging stresses, (b) bridging stress distribution versus crack opening displacement, δ.

bone and dentin (Kruzic et al., 2003; Nalla et al., 2005). When modeling the effects of bridging on the fracture behavior it is generally useful to adopt a continuum approach. This effectively smooths out the many discrete load bearing bridges into a continuous bridging stress distribution $\sigma_{br}(\delta)$ (Fig. 1) where the bridging stresses depend on the local crack opening displacement δ (Fett et al., 1995; Foote et al., 1986; Raddatz et al., 1998). This relationship is widely believed to represent a true material property uninfluenced by sample geometry, loading conditions, and other extrinsic factors. As such, it substantially controls the mechanical properties of these materials and can be used in conjunction with fracture mechanics weight functions to evaluate mechanical properties that are dependent on geometry and loading conditions such as fracture resistance curves (R-curves) for different crack geometries (Fett et al., 2008a).

Many techniques have been employed to measure bridging stress distributions and they may be broadly classified as non-destructive or destructive. The multi-cutting compliance technique is destructive and involves measuring the compliance after incremental saw cuts are made into the wake of a bridged crack (Hu et al., 1991; Hu and Mai, 1992; Kruzic et al., 2004). Another destructive approach is to machine small post fracture tensile specimens by sectioning larger cracked ceramic or fiber composite specimens (Geraghty et al., 1999; Hay and White, 1993; Walls and Zok, 1994; White and Hay, 1994). The post fracture specimens are oriented such that they span the crack wake of the larger specimen and thus each one contains a portion of the original bridged, through-thickness, crack which can then be tensile tested. In addition to these techniques being destructive, another limitation is their spatial resolution which is limited by the size scale of the micromachining needed to make the incremental cuts or post fracture specimens.

Conversely, several non-destructive techniques for determining bridging stresses involve calculations using weight functions (Fett, 1995a, b, 1995). The relationship between crack opening displacement and stress allows bridging stress profiles to be computed from crack opening displacement (COD) profiles (Fett, 1995b), which can be measured using various methods such as with a scanning electron or atomic force microscope. For this method, the sample must be held under an applied crack opening load which leads to several instrumentation difficulties. Another limitation of the COD based method is that COD profiles can be difficult to accurately measure — especially for small or tortuous cracks.

The relation between the stress intensity factor and the bridging stresses also allows the bridging stress profile to be determined directly from the measured R-curve (Fett, 1995a; Fett et al., 1995). While such methods have been traditionally very computationally expensive, recently approximations have been developed that significantly reduce the computational time (Fünfschilling et al., 2010a, 2011). The accuracy of R-curve based methods can be limited by the ability to accurately measure the most important initial portion of steeply rising R-curves (Fünfschilling et al., 2010b; Kruzic et al., 2008). Overall, weight function based techniques have been applied to a wide range of fiber reinforced composites and monolithic ceramics (Buchanan et al., 1997; Cox and Marshall, 1991; Fett, 1995a, b; Fett et al., 2000, 2005a; Gilbert and Ritchie, 1998; Kruzic et al., 2004; Pezzotti et al., 1999b; Sorensen et al., 2008; Studer et al., 2003).

Light spectroscopy methods (e.g., Raman or fluorescence based) are also non-destructive and have been frequently used to measure bridging stresses in various ceramics, composites, and even bone where specific spectrum peaks are affected by stress. Fluorescence spectroscopy is a common method for determining stresses in Al_2O_3 containing materials by measuring the shift from their stress-free position in the characteristic R1 and R2 Cr^{3+} optical fluorescence lines produced by chromium impurities (Dauskardt and Ager, 1996; He and Clarke, 1995). Since chromium is a ubiquitous substitutional impurity in alumina and sapphire, microprobe fluorescence spectroscopy has been used successfully for measuring bridging stresses in alumina and alumina-containing composites by moving a focused laser along the bridging zone of the crack (Belnap and Shetty, 1998, 2005; Pezzotti et al., 1999b, 1998, 1999c). A limitation of this technique is that the material to be studied must fluoresce and to date studies have been generally limited to alumina-containing materials.

Similarly, certain Raman spectrum peaks shift to lower wave numbers by the application of tensile stress. Accordingly, Raman microprobe spectroscopy has been employed in a manner similar to fluorescence techniques to determine bridging stress profiles in a wider range of materials including fiber reinforced polymer and ceramic matrix composites, Si_3N_4 ceramics, and even bone (Bennett and Young, 2008; Dassios et al., 2003; Kruzic et al., 2005a; Pezzotti, 1999; Pezzotti et al., 2001, 1999a; Pezzotti and Sakakura, 2003). Some limitations of Raman spectroscopy are that it cannot generally be used for metallic materials because fluorescence signals from the material or impurities hide the relatively weak Raman signal.

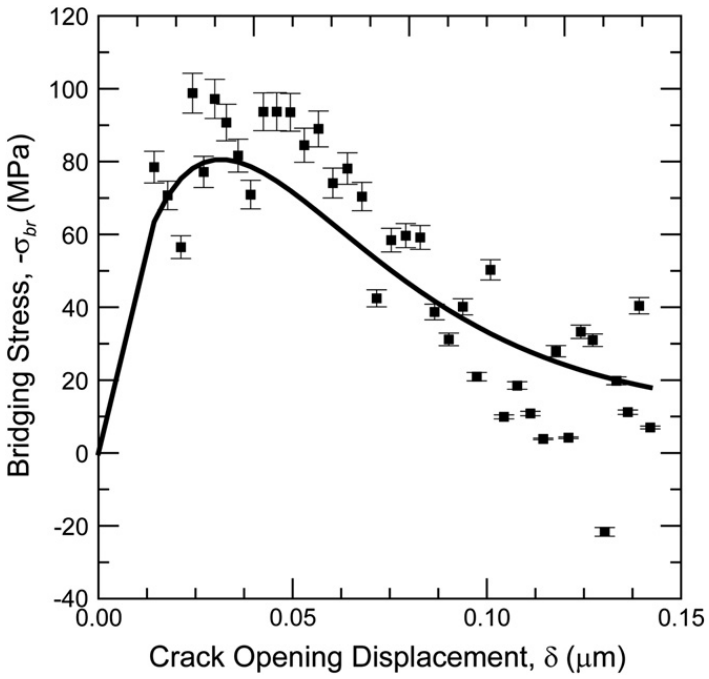

Fig. 2. Fatigue crack bridging stress distribution for a 99.5% pure Al_2O_3 calculated from weight functions and the fatigue threshold *R*-curve (solid line). Also plotted are bridging stresses measured using fluorescence spectroscopy (solid circles) with error bars indicating ± 1 standard deviation based on the standard deviation of the linear calibration fit. Reprinted from Gallops et al. (2011a) with permission from Elsevier.

Another challenge is that data collection times can be long relative to fluorescence potentially causing data scatter due to thermal drift of the peak.

Finally, another non-destructive technique involves using synchrotron X-ray micro-diffraction to measure local crystal lattice strains, such as has been used in titanium matrix composites (Preuss et al., 2003). A major advantage of this technique is that any crystalline material can be studied; however, the necessity for a synchrotron X-ray source makes this technique impractical for day-to-day measurements of bridging stress distributions. Also, common to X-ray diffraction and light spectroscopy microprobe methods is that the sample must be held under an applied crack opening load which requires specialized in-situ testing stages and may result in subcritical crack growth affecting the results.

Despite the large amount of research on bridging stresses, to date there is a scarcity of information on how the results from various methods compare to one another. One recent comparison of independently measured bridging stresses for an Al_2O_3 ceramic is very encouraging (Gallops et al., 2011a). Indeed, bridging stresses for a fatigue crack were determined by fluorescence spectroscopy and from the *R*-curve and the results agreed well (Fig. 2).

However, there are many challenges to accurately determining bridging stresses that will be addressed in the present paper. Accordingly, it is the goal of this paper to compare results from several non-destructive techniques that are relatively easy to implement in most laboratories, including the calculation of bridging stresses from *R*-curves and CODs and both fluorescence and Raman micro-spectroscopy. New results are presented for Si_3N_4 and Al_2O_3 ceramics and are compared with published results for both *R*-curve and fatigue generated cracks. Furthermore, a new method is proposed for deducing the bridging stress distribution for fatigue cracks in situations where other methods have been found to be problematic. The results of this study provide new insight into the limitations and advantages of the various techniques and will aid researchers in choosing appropriate methods for given situations.

2. Experimental methods

2.1. Materials

Bridging stresses are examined for two different materials: a hot-isostatically pressed silicon nitride containing 5 wt% Y_2O_3 and 2 wt% MgO as sintering aids and a commercial 99.5% pure Al_2O_3 (CoorsTek AD995). Full details on the processing of the silicon nitride may be found elsewhere (Satet and Hoffmann, 2005), but briefly, powders were prepared by attrition milling in isopropanol and the slurries were subsequently dried and the powders sieved. Green bodies were uniaxially pressed and then subsequently cold-isostatically pressed at a pressure of 400 MPa. The samples were sintered in a hot-isostatic-press (HIP) with a two-step sinter-HIP process, where closed porosity is obtained at low N_2 pressures during the first sintering step and full density was achieved during the subsequent HIP step at a maximum nitrogen pressure of 10–20 MPa. Full density (water immersion method) is defined here for relative densities greater than 99% of theoretical density, which was calculated by the rule of mixture based on the starting compounds. The silicon nitride features

elongated β-phase grains with an average diameter of 0.28 μm with an aspect ratio of ~7. The alumina ceramic is the same as in Fig. 2 and in Gallops et al. (2011a, 2011b). It has nominally equiaxed grains widely ranging in size with a majority having cross-sectional areas of $<63\ \mu m^2$ (or diameter of $<9\ \mu m$). Information on the grain size distribution may be found in Gallops et al. (2011b).

2.2. Bridging stresses from crack opening displacements (CODs)

A procedure that allows the bridging stresses to be determined from crack opening displacement (COD) measurements was developed previously (Fett, 1995b). The bridging stresses σ_{br} acting against crack opening depend on the opening displacements δ. From the measured R-curves the bridging stress intensity factor K_{br} is known since

$$K_R = K_{I0} - K_{br}, \quad K_{br} < 0 \tag{1}$$

Any stress intensity factor can be represented by a stress distribution acting in the wake of the crack (Fig. 1(a)). Accordingly, using the weight function representation the bridging stress intensity factor is given by

$$K_{br}(\Delta a) = \int_0^{\Delta a} h(r,a)\sigma_{br}(r)\mathrm{d}r \tag{2}$$

with the fracture mechanics weight function h for the appropriate geometry (Fett and Munz, 1997), the distance r from the tip, the initial crack length a_0 free of bridging, and the crack extension, $\Delta a = a - a_0$. The total crack opening displacement δ can be computed as the sum of the displacement that would occur due to an applied load for non-bridging specimen δ_{appl} and the displacement (which is a negative value) due to the effects of the bridging toughening mechanism δ_{br} by

$$\delta = \frac{1}{E'}\int_{a-r}^{a} h(r,a')K_{appl}(a')\mathrm{d}a' + \frac{1}{E'}\int_{a-r}^{a} h(r,a')\left[\int_{a-r}^{a'-a_0} h(r',a')\sigma_{br}(r')\mathrm{d}r'\right]\mathrm{d}a' \tag{3}$$

Using Eqs. (1)–(3) the bridging stress distribution $\sigma_{br}(\delta)$ may be determined. For this purpose the simple set-up for the unknown relation can be made by

$$\sigma_{br} \approx \sum_{(n)} \sigma_n \frac{\delta}{\delta_n}\exp\left[\frac{-\delta}{\delta_n}\right] \tag{4}$$

This bridging stress relation is inserted into Eqs. (2) and (3). A solution of this system of integral equations is found by systematic variation of the free parameters in (4) under the condition that the resulting $\delta(r)$ function must coincide with the measured CODs and thus provide the best set of unknown parameters σ_n and δ_n.

To compare with bridging stress results determined from fracture R-curves published in the literature for notched bend beams (Fünfschilling et al., 2009b, 2011), the above procedure was used to determine $\sigma_{br}(\delta)$ for a Si_3N_4 compact tension sample used to measure a fracture toughness R-curve in a previous paper (Kruzic et al., 2008). The K_{I0} value used (2.3 MPa$\sqrt{m}$) was taken from the published literature and determined from the crack tip opening displacements of Vickers indent cracks (Fünfschilling et al., 2009a).

2.3. Fatigue threshold experiments

New fatigue threshold experiments were conducted for the Si_3N_4 material using standard compact-tension, C(T), specimens (width, $W \approx 19$ mm; thickness, $B \approx 3.5$ mm) in general accordance with ASTM standard E647 (ASTM, 2010). More complete details of the fatigue-crack growth procedures are in Kruzic et al. (2005a, 2004) while a brief summary of issues pertinent to the measurement of fatigue thresholds is presented here. Fatigue cracks were initiated from straight machined notches (length $a_0 \approx 4$–5 mm) under cyclic loading conditions ($\nu = 25$ Hz frequency sine wave, load ratio, $R = P_{max}/P_{min} = 0.1$), after which the cracks were grown while monitoring crack length using back-face strain compliance methods (Deans and Richards, 1979). Specimens were razor micro-notched to have root radii, $\rho < 10$ μm. This was done by repeatedly sliding a razor blade over the notch in the presence of a 1 μm diamond paste. Data collection did not begin until the crack was growing evenly (both sides within 10% of each other) and the amount of fatigue-crack extension from the notch, Δa_f, exceeded ρ, at which point the influence of the notch field on the stress intensity could be considered to be negligible (Dowling, 1979; Palazotto and Mercer, 1990).

Fatigue crack growth rates were measured as a function of the applied stress intensity range, $\Delta K = K_{max} - K_{min}$, where K_{max} and K_{min} are the maximum and minimum stress intensity applied during the loading cycle. In order to measure the fatigue threshold, the applied stress-intensity range was reduced at a roughly constant ΔK-gradient ($=[d\Delta K/da]/\Delta K$) of $-0.08\ mm^{-1}$. In this manner the fatigue threshold ΔK_{TH} was taken as the lowest stress intensity at which the fatigue-crack growth rate could be measured and does not exceed $\sim 10^{-10}$ m/cycle. For this Si_3N_4 material the bridging zone is known to be only tens of micrometers in length (Fünfschilling et al., 2009b, 2011). Thus, a determination of fatigue thresholds during the bridging zone development and the fatigue threshold R-curve $\Delta K_{TH}(\Delta a)$, as was done in Gallops et al. (2011a) for Al_2O_3, was impossible. Rather, the steady state fatigue threshold, ΔK_{TH}, was determined for a fully developed bridging zone.

2.4. Spectroscopy

2.4.1. Bridging stress measurements

The Raman microprobe technique was used to measure bridging stresses for C(T) fatigue samples that were last tested near the fatigue threshold. The specimens were re-loaded in situ to ~95% of the K_{max} value at the measured fatigue threshold K_{TH}^{max}. A 488-nm laser was focused using an optical microscope with a 50*X* objective to a ~1 μm spot size on the sample surface. Laser power at the surface was kept below 7 mW to avoid measurement drift due to sample heating. Scattered light was directed through a holographic laser line filter and into a 640 mm single spectrometer using a liquid-nitrogen cooled, back-thinned CCD camera. There were two different colors of silicon nitride specimens: black and light-grey. Their mechanical properties were unaffected by color but the optical properties deemed that longer exposures were required for the darker specimens. For the darker specimens 360 s exposures were used while for the lighter color specimens only 120 s exposures were required to get equivalent peak intensity. The longer time was needed in the former case due to a smaller laser probe sampling volume (described below) and thus fewer backscattered Raman photons exiting the sample per second.

Peak shifts in silicon nitride were first measured along the crack wake at small increments of 2 μm starting ahead of the crack tip to focus on the detail of the peak bridging stresses. Larger increments of 4 and 6 μm were used as measurements progressed along the crack wake until bridging stresses decreased to zero after about 200 μm. Effects due to ambient temperature variations and/or instrument drift were minimized by recalibrating using an internal zero stress reference (a part of the sample far away from the crack). These zero points were taken after every ~5 measurements.

Results were analyzed in an identical fashion. First, any spikes in the spectra due to cosmic rays were removed manually and then a seven-point, third-order Savitsky–Golay smoothing method was applied. A rolling-ball technique was then adopted to remove the background (Sternberg, 1983). Next, the peak of interest was isolated from the rest of the spectrum and a Gaussian curve-fit was used to determine the peak location in cm^{-1}. In order to calculate the peak-shift, the zero stress peak position corresponding to each bridging stress measurement was determined by simple linear interpolation between the associated calibration points before and after the measurement. The peak-shift was then the difference of the measured peak location and its associated zero calibration. The bridging stress at each point was determined by dividing the calculated shift by a calibration factor and then linearly scaling the stress up to 100% to account for loading the sample to only 95% of the maximum load at threshold. A series of experiments were conducted at different loading levels to verify that this liner extrapolation was a reasonable approximation.

The resulting bridging stress values from Raman results were fitted according to

$$\sigma_{br} = \sigma_0 \frac{r}{r_0} \exp\left(\frac{-r}{r_0}\right) + \sigma_1 \frac{r}{r_1} \exp\left(\frac{-r}{r_1}\right) \tag{5}$$

and then converted to terms of δ using the Irwin approximation for the near-tip behavior ($r \to 0$)

$$\delta_{tip} = \sqrt{\frac{8r}{\pi}} \frac{K_{I0}}{E'} \tag{6}$$

2.4.2. Stress calibration

Because the stress dependence of the Raman shift of the 862 cm^{-1} peak for Si_3N_4 can be affected by changes in chemical composition (Pezzotti, 1999) a calibration was performed for our sample composition using a 2 mm by 3 mm cross-section beam in three-point bending at a peak stress of ± 500 MPa. The laser was moved in 160-μm increments along the bend beam to record the peak shift with changing stress, again using an internal zero stress reference, as described above, which was recalibrated every five measurements. This calibration gave an average piezo-spectroscopic coefficient Π_{avg} of -1.57 ± 0.22 cm^{-1}/GPa. This value falls near those obtained by Pezzotti et al. for Si_3N_4 materials sintered with Al_2O_3 which contain SiAlON phases (-1.63 to -1.69 cm^{-1}/GPa) (Pezzotti, 1999; Pezzotti et al., 1999a).

2.4.3. Sampling volume determination

To allow a comparison of the present Raman spectroscopy results for Si_3N_4 with the fluorescence spectroscopy results shown in Fig. 2 from Gallops et al. (2011a) the laser sampling volumes were determined for both materials. The sampling volumes were calculated based on the absorption coefficients measured using thin samples. To analyze the absorption of the silicon nitride a green laser (λ=533 nm) was used. This laser is near both the probe wavelength (488 nm) and the wavelength of the Raman peak (510 nm) to give a reasonable estimate of the absorption coefficient. For the absorption of alumina both the green light absorption and red light absorption was examined. The fluorescence peak of alumina occurs at about 677 nm and the second laser used had a wavelength of about 680 nm. It was determined that the absorption at 533 nm was the limiting factor; accordingly, that laser was used for both materials.

The intensity of the transmitted laser light was measured after passing through thin sections of material using a custom specimen holder. For Si_3N_4, which is opaque, thin sections of 42–79 μm were used. For Al_2O_3, which is translucent, thicker sections of 813 and 1096 μm were used. A Newport Digital Power Meter (Model 815 series) along with a Newport 818-L photodetector was used to measure the intensity change. In addition, a Newport 883-SL OD3 optical attenuator was used

to extend the range of the photodetector by a factor of 1000. The absorption coefficient was calculated using Beer's Law:

$$\frac{I}{I_0} = e^{-\alpha t} \tag{7}$$

where I is the intensity of the incident light, I_0 is the intensity of the transmitted light, α is the absorption coefficient, and t is the thickness of the specimen. The Raman probe depth was then calculated by the simple relation

$$\text{depth} = \frac{1}{2\alpha} \tag{8}$$

By applying a Gaussian beam approximation the shape of the sampling volume of the laser in the material was estimated. The shape of the beam spread into the material $w(z)$ was calculated using the following,

$$w(z) = w_0\sqrt{1+\left(\frac{z\lambda}{\pi w_0^2}\right)^2} \tag{9}$$

where w_0 is the beam waist, or half the spot diameter focused on the surface of the sample, z is the depth into the sample, and λ is the wavelength of the probe laser. The shape of the maximum penetration of the laser was assumed to be a simple circular arc. Sampling volume was determined by integration of the beam profile about the axis of penetration.

3. Results

3.1. Bridging stresses from crack opening displacements and R-curves (Si_3N_4)

Fig. 3(a) shows crack opening displacement measurements on the side surface of an C(T) specimen previously used in Kruzic et al. (2008) to measure a fracture R-curve under a monotonically increasing load. The open circles represent the CODs for a sample held at roughly 97.5% of the maximum load where K_R=6.76 MPa $\sqrt{m}$, i.e., at 6.59 MPa $\sqrt{m}$. For the evaluation of these data, the weight function for the C(T) specimen was used in Eq. (3) as available from fracture mechanics handbooks (e.g., Fett and Munz, 1997).

The measured surface data are obtained under plane stress conditions. The dashed curve in Fig. 3(a) shows δ_{appl}. Solution of Eq. (3) yields the displacements given by the solid curve in Fig. 3(a) that matches the experimental data (circles). The final result of the computations, namely $\sigma_{br}(\delta)$, is represented in Fig. 3(b) as the solid curve. In addition, Fig. 3(b) shows the result directly from the R-curve measured using a notched four-point bend beam specimen (Fünfschilling et al., 2009b, 2011). Analysis for the C(T) R-curve from Kruzic et al. (2008) was not conducted because that R-curve rises very steeply and the C(T) technique did not measure the rising portion adequately. This shortcoming prompted the development of new R-curve methods using bend beams described in detail in Fünfschilling et al. (2010b).

The comparison of the bridging laws exhibits rather strong differences. The peak bridging stress from COD measurements is significantly lower than with the the R-curve evaluation. The peak stresses are −1700 MPa for the notched bending bar and −1200 MPa for the CT-specimen. In this context, it has to be mentioned that the bridging stresses from the R-curve evaluation was considered more sensitive than the COD evaluation due to the higher spatial resolution of the data collection that was possible for the smallest opening displacements.

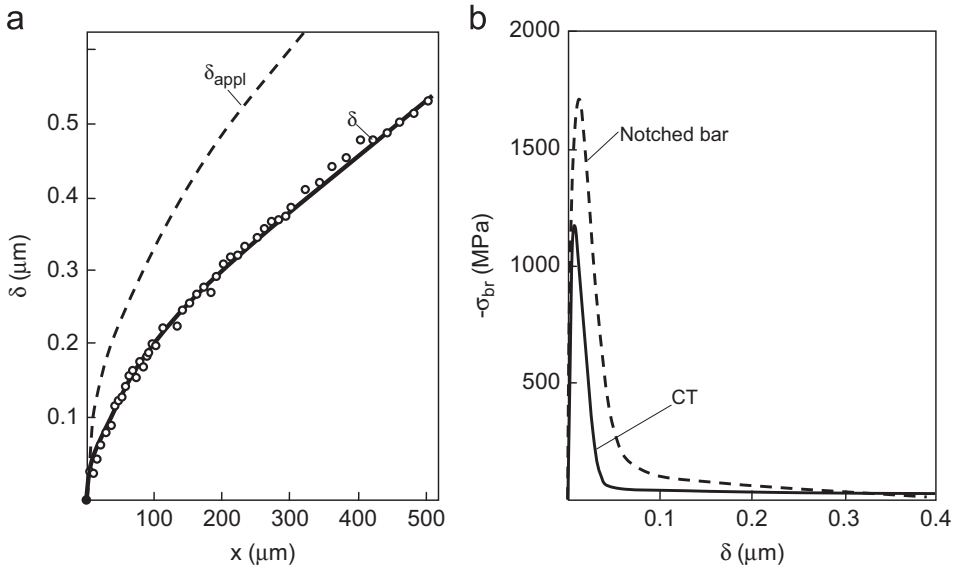

Fig. 3. (a) COD results at the surface of a crack in a C(T) specimen (circles: measurements, dashed curve: applied displacements δ_{appl}, solid curve: result of Eq. (3) matched to the measured data), (b) bridging stresses for the different test specimens.

3.2. Fatigue crack bridging stress results (Si_3N_4)

Based on six fatigue threshold experiments using five C(T) samples a mean $\pm$ standard deviation fatigue threshold of $\Delta K_{TH} = 4.1 \pm 0.2$ MPa$\sqrt{}$m was determined. There was no significant difference between the differently colored samples. Fig. 4(a) shows example Raman bridging stress data collected for an individual black silicon nitride fatigue specimen along with its curve fit using Eq. (5). Fig. 4(b) shows all curve fits for the black and light-grey silicon nitride fatigue samples. As can be seen, all of the black sample data lies at much higher stress values than the light-grey specimens. The light-grey specimens also exhibit much less scatter.

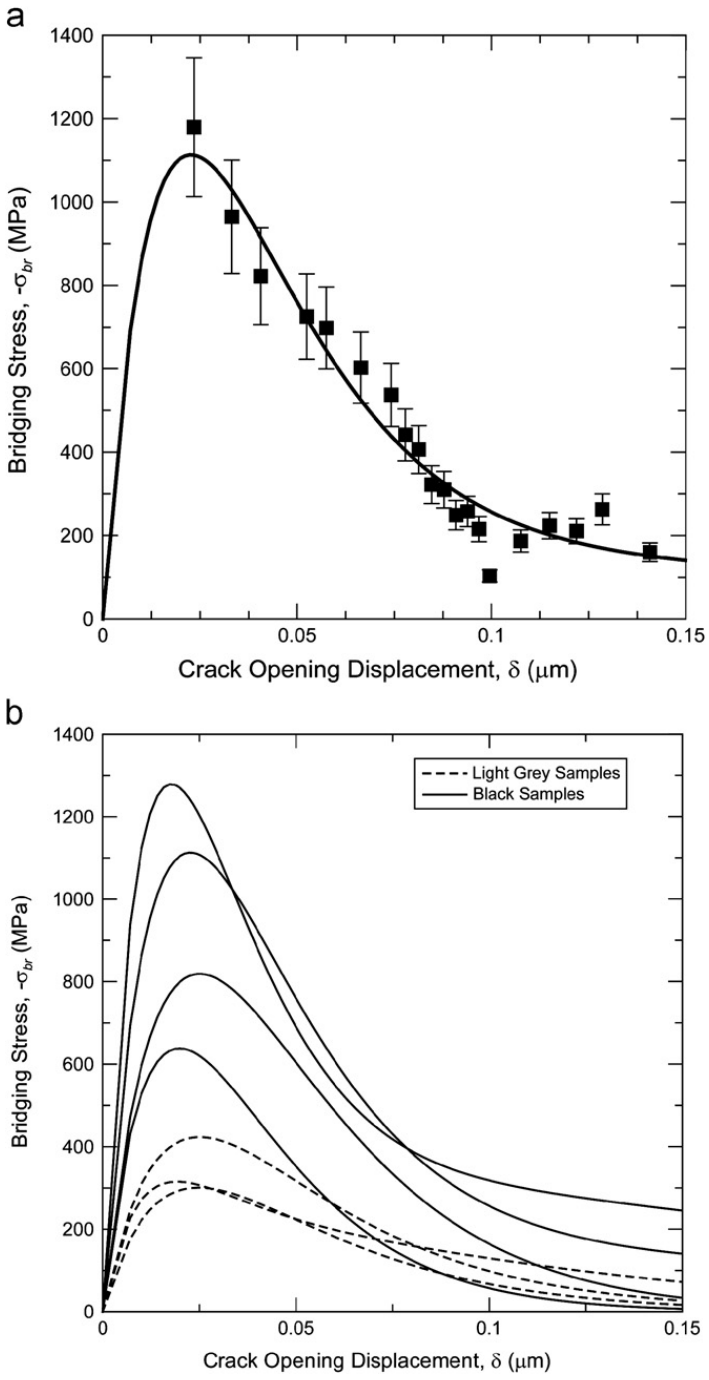

Fig. 4. (a) Bridging stress distribution data determined for a single specimen along with the associated fit using Eq. 5. Error bars indicate the standard deviation for the calibration constant. (b) Fits of the bridging stress data for all specimens showing the difference in peak stress between the light-grey and black specimens.

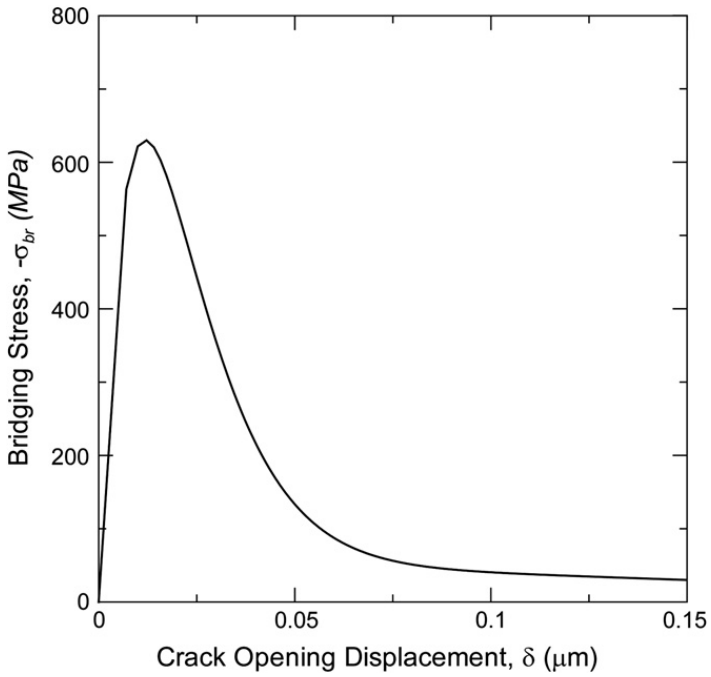

Fig. 5. The deduced best estimate of the fatigue threshold crack bridging stress distribution for Si_3N_4.

3.3. Estimating the fatigue threshold bridging stress distribution for Si_3N_4

Due to the high degree of scatter in the stress distributions shown in Fig. 4(b), a best estimate of bridging stresses for fatigue in silicon nitride was deduced as shown in Fig. 5. This distribution was obtained by reducing the peak magnitude of the published bridging stress distribution obtained from *R*-curve fracture experiments (Fünfschilling et al., 2010b) to account for the fatigue degradation of the bridging stresses in the present case. It was decided to use these data because they were collected using the most sensitive measurement method for the smallest crack openings and thus it is expected the distribution shape is most accurate. Also, as will be discussed below the *R*-curve method gives a better through thickness average of the bridging stresses than the surface sensitive COD method. Since the peak stress is being lowered, the differences in peak magnitudes between methods are not a significant concern. The maximum stress intensity of the loading cycle at the fatigue threshold,

$$K_{\mathrm{TH}}^{\max} = \Delta K_{\mathrm{TH}}/(1-R) \tag{10}$$

was calculated and used as a known value to decrease the magnitude the bridging stress distribution until the correct value of K_{br} was achieved via Eq. (2) noting that $K_{\mathrm{br}} = K_{I0} - K_{\mathrm{TH}}^{\max}$ (where $K_{\mathrm{br}} < 0$) according to Eq. (1). The crack tip toughness, K_{I0}, was again taken to be 2.3 MPa$\sqrt{\mathrm{m}}$.

Fig. 6 compares the averages for the light-grey, black, and all specimens as well as the deduced best estimate of the fatigue-threshold bridging stress distribution from Fig. 5. Of interest to note is that the best estimate and the total sample average have a similar peak stress values, while the best estimate and light-grey average have similar areas under their curves.

3.4. Sampling volume results

The sampling volume for silicon nitride differed based on the color of the material. The volume for the light grey specimens was determined to be 56 μm^3 with a depth of 7.2 μm equating to ~25 average grain diameters. For the black specimens the volume was 30 μm^3 with a depth of 5.0 μm equating to ~18 average grain diameters. These depths of penetration correspond to only ~0.1–0.2% of the total sample thickness. The sampling volume for alumina was calculated to be 23,645 μm^3 with a depth of 84 μm, or ~2.5% of the total sample thickness. Fig. 7(a) shows the laser sampling volume cross-section for the silicon nitride samples and Fig. 7(b) shows the sampling volume cross-section for the alumina samples compared to that of the silicon nitride samples. For the alumina samples the percentage of the thickness sampled was more than an order of magnitude higher than for the Si_3N_4 samples.

4. Discussion

Two types of cracks have been examined in this study, those produced under monotonically increasing loading conditions and those produced under cyclic fatigue loading conditions. From the perspective of bridging stresses the

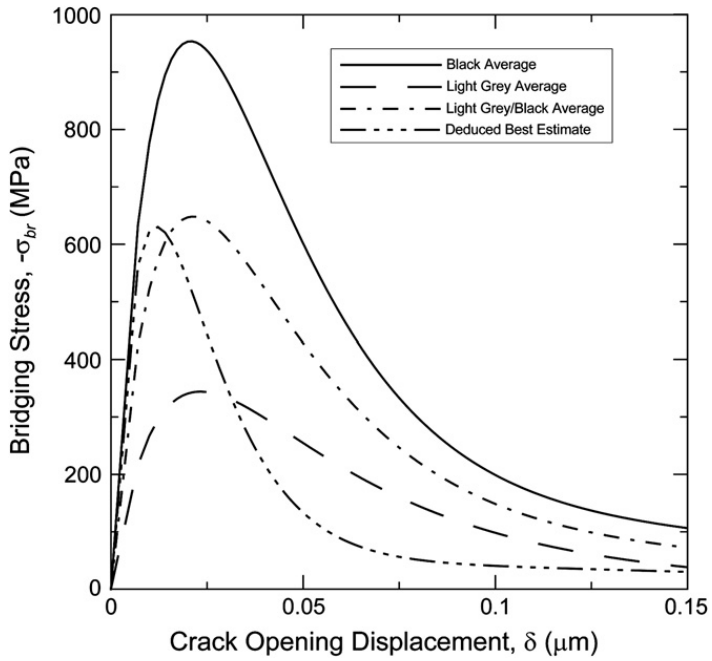

Fig. 6. A comparison of the average Raman determined fatigue threshold crack bridging stress distributions for Si_3N_4. Averages for the black samples (solid line), light grey samples (dashed line), and all samples (dash-dot line) are shown. Also shown is the deduced best estimate from Fig. 5 (dash-triple-dot line).

fatigue cracks should always show lower peak bridging stress magnitudes due to the cyclic degradation of bridges. A quick comparison of Figs. 4(b) and 6 demonstrate this clearly. However, it is expected that bridging stress results should be consistent for a specific type of crack, as has been shown for alumina in Fig. 2 (Gallops et al., 2011a).

From the present results it is apparent that several difficulties can occur when determining the bridging stresses for Si_3N_4. First, two different peak stresses were obtained for bend and C(T) samples for cracks grown under monotonically increasing loading conditions. Second, the bridging stresses measured using Raman spectroscopy were highly scattered in peak stress from sample to sample, especially for the darker samples. The following discussion will focus on explaining these phenomena.

4.1. *Effect of the free surface*

A model for the bridging mechanism in silicon nitrides with very steep *R*-curves was proposed in Fünfschilling et al. (2011). These Si_3N_4 ceramics consist of 100% β-phase crystals with needle-like grains of high aspect ratio. Such a needle with length axis oriented at an angle of Θ relative to the plane of a crack terminating at the elongated crystal is schematically shown in Fig. 8(a). A free surface must have an important influence on the bridging stresses because the grains located close to this surface undergo a reduced "clamping" force by residual stresses caused by thermal expansion anisotropy of the grains. The consequence is increased debonding and the generation of a free neck around the crystal circumference which results in a more compliant structure at the surface.

Due to the missing thermal mismatch stress component normal to the free surface (Fig. 8(b)) also the pull-out resistance of the frictional bridges is reduced as can be concluded from the friction model by Mai and Lawn (1987), Fig. 8(c). Note that the illustration in Fig. 8(c) shows a $\Theta = 90^\circ$ oriented pullout for simplicity while most actual pullouts will be at an inclined angle.

According to the theorem of Saint Venant, the reduction of mismatch stresses is restricted to a very thin zone of only a few grain diameters in thickness. Therefore, COD measurements at the surface must yield excessive displacements that will underestimate the bridging stresses according to Eq. (3). This factor can, in part, explain the lower bridging stresses deduced from the COD method relative to the *R*-curve method (Fig. 3(b)).

4.2. *Effect of the T-stress and sample geometry*

Considering the expected influence of the free surface on bridging stresses determined from COD method, the *R*-curve method provides an attractive alternative since a through thickness averaged bridging stress distribution is determined. Accordingly, it is expected highly accurate results are obtained when the crack not influenced by the starter notch, as for the alumina data shown as the solid line in Fig. 2. However, for the special case of materials with steeply rising *R*-curves (e.g., Si_3N_4) the *R*-curve measurements must be made while the crack is still under the influence of the starter notch stress field. In that case there can be effects of the *T*-stress on the determined bridging stress distribution, as described below.

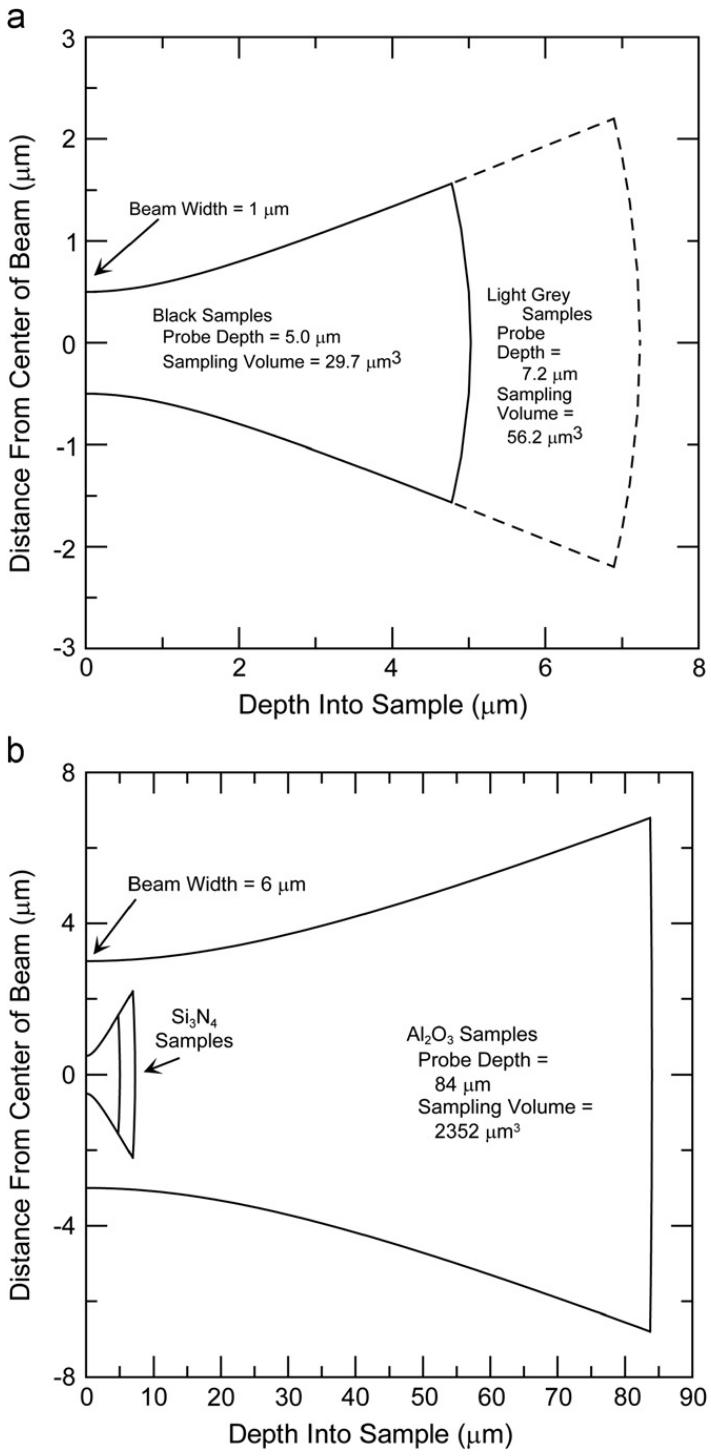

Fig. 7. (a) A comparison of the Raman spectroscopy sampling volumes for the black and light grey Si_3N_4 samples. (b) A comparison of the Raman sampling volume for the Si_3N_4 samples with the fluorescence sampling volume for the Al_2O_3 samples.

If K_I denotes the mode-I stress intensity factor, the crack-parallel near-tip stresses σ_x represented by the singular and the first regular stress terms are written as

$$\sigma_x = \frac{K_{\text{tip}}}{\sqrt{2\pi r}} \cos\tfrac{1}{2}\varphi\left(1-\sin\tfrac{1}{2}\varphi\sin\tfrac{3}{2}\varphi\right)+T+O(r^{1/2}) \tag{11}$$

where r is the crack-tip distance and φ the polar coordinate angle. In the wake of the crack where the bridging interactions are active $\varphi=\pi$ and only T, the crack-parallel so called "T-stress," remains fully present. Its influence may be discussed using a simplified model.

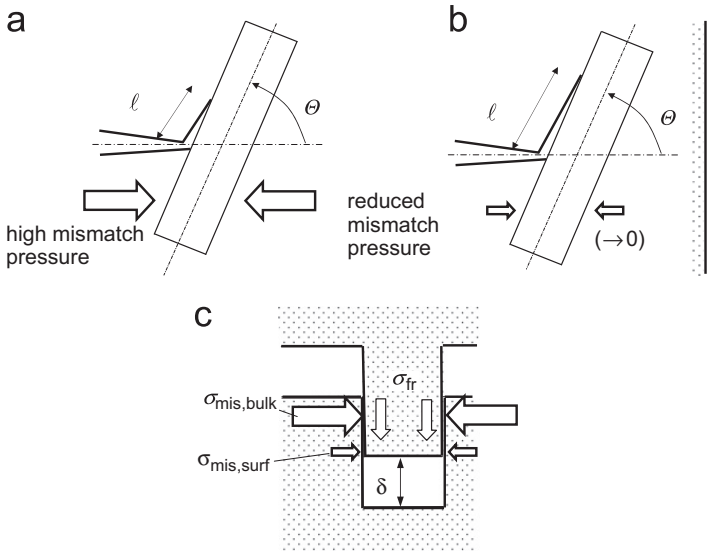

Fig. 8. Influence of a reduced compressive stress normal to a β-crystal. Debonding lengths under the same externally applied load for (a) bulk material, (b) grains located near a free surface (c) Crack surface interaction due to a local frictional bridging event and frictional stress σ_{fr} which is affected differently by the bulk and surface mismatch stresses, $\sigma_{mis,bulk}$ and $\sigma_{mis,surf}$, respectively.

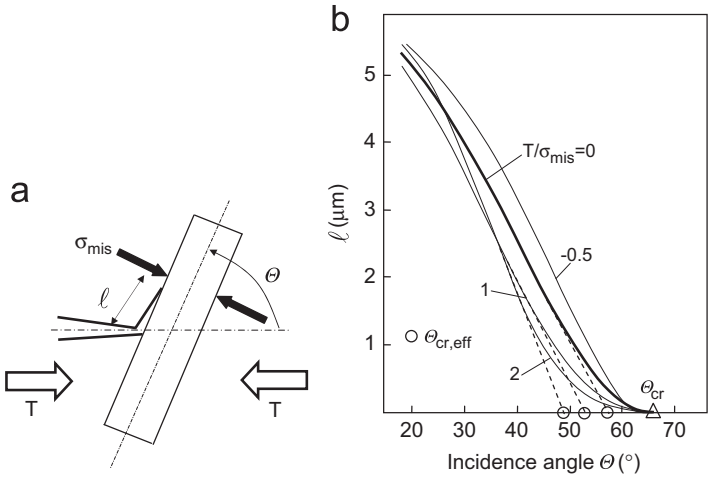

Fig. 9. Influence of T-stress on debonding, (a) crack kinking at the interface grain/grain-boundary phase, (b) effect of $T \neq 0$ on debonding length.

Due to the anisotropy and non-homogeneity of a Si_3N_4-ceramic, the computation of stress intensity factors for the kink situation in Fig. 8(a) is very complicated. The K-values are complex numbers. In order to allow a simple understanding of the trends caused by the T-stress, an approximation may be made by assuming a unique isotropic and homogeneous Young's modulus and Poisson's ratio.

The effect of a debond of length ℓ occurring for an angle of $\Theta < \Theta_{cr}$ is shown in Fig. 9(a). Θ_{cr} is the critical angle that defines the debonding versus non-debonding conditions. The crack may terminate in the center of a β-grain where shear-mismatch disappears due to symmetry. Kinks into the weaker direction of the grain boundary can develop under the superimposing normal component of the thermal mismatch stress, $\sigma_{mis} < 0$, and the T-stress T resulting in a kink of length ℓ. The stress intensity factors at the tip of the kink can then be written

$$K_I(\ell) = K_I(a)\cos^3(\tfrac{1}{2}\Theta) + \sigma_{mis}\sqrt{\ell}\sqrt{\frac{8}{\pi}} + T\sqrt{\ell}\sqrt{\frac{8}{\pi}}\sin^2\Theta \tag{12a}$$

$$K_{II}(\ell) = K_I(a)\cos^2(\tfrac{1}{2}\Theta)\sin(\tfrac{1}{2}\Theta) - T\sqrt{\ell}\sqrt{\frac{8}{\pi}}\sin\Theta\cos\Theta \tag{12b}$$

where the mode-I stress intensity factor $K_I(a)$ and the T-stress T are computed for the straight unkinked crack (i.e., for $\ell \to 0$). The energy release rate for crack extension by ℓ can be represented by an effective stress intensity factor K_{eff}

$$G = K_{\text{eff}}^2/E', \quad E' = E/(1-\nu^2) \tag{13a}$$

$$K_{\text{eff}} = \sqrt{K_I(\ell)^2 + K_{II}(\ell)^2} \tag{13b}$$

A kink along the interface must grow until K_{eff} equals the "fracture toughness" $K_{\text{Ic,int}}$ of the interface. The kink length ℓ can be quantified in terms of the two parameters $\sigma_{\text{mis}}/K_I(a)$ and T/σ_{mis} by solving the equation

$$\left(\frac{K_{\text{Ic,int}}}{K_I(a)}\right)^2 = \left(\cos^3(\tfrac{1}{2}\Theta) + \frac{\sigma_{\text{mis}}}{K_I(a)}\sqrt{\ell}\sqrt{\frac{8}{\pi}}\left(1 + \frac{T}{\sigma_{\text{mis}}}\sin^2\Theta\right)\right)^2 + \left(\cos^2(\tfrac{1}{2}\Theta)\sin(\tfrac{1}{2}\Theta) - \frac{\sigma_{\text{mis}}}{K_I(a)}\frac{T}{\sigma_{\text{mis}}}\sqrt{\ell}\sqrt{\frac{8}{\pi}}\cos\Theta\sin\Theta\right)^2 \tag{14}$$

For $\ell = 0$ the critical incidence angle Θ_{cr} results from

$$\frac{K_{\text{Ic}}}{K_I(a)} = \cos^2(\tfrac{1}{2}\Theta_{\text{cr}}) \tag{15}$$

For any given incidence angle Θ the kink length ℓ can be determined as the zeros of

$$\cos^4(\tfrac{1}{2}\Theta_{\text{cr}}) = \left(\cos^3(\tfrac{1}{2}\Theta) + \frac{\sigma_{\text{mis}}}{K_I(a)}\sqrt{\ell}\sqrt{\frac{8}{\pi}}\left(1 + \frac{T}{\sigma_{\text{mis}}}\sin^2\Theta\right)\right)^2 + \left(\cos^2(\tfrac{1}{2}\Theta)\sin(\tfrac{1}{2}\Theta) - \frac{\sigma_{\text{mis}}}{K_I(a)}\frac{T}{\sigma_{\text{mis}}}\sqrt{\ell}\sqrt{\frac{8}{\pi}}\cos\Theta\sin\Theta\right)^2 \tag{16}$$

For a critical incidence angle of $\Theta_{\text{cr}} = 65^\circ$, the kink length as a function of the kink angle is plotted in Fig. 9(b) for the case $T = 0$ by the bold line. This result was obtained from Eq. (16) with a parameter of $\sigma_{\text{mis}}/K_I(a) = -73\sqrt{\text{m}}$ that matches the value $\ell = 5.3$ μm at $\Theta = 18^\circ$ as found by Kruzic et al. (2008) for a Si_3N_4-ceramic with similar microstructure but La doping instead of Y. The thin lines represent the effect of the T-stress. Since the mismatch stress is negative, the ratio T/σ_{mis} is positive for a negative T-stress. The linear extrapolation of the lower curve parts to $\ell \to 0$ defines effective critical kink angles indicated by the circles. With increasing T/σ_{mis} these effective critical kink angles, designated now as $\Theta_{\text{cr,eff}}$, decrease.

Since $K_I(a)$ should be in the order of $5 < K_R < 7$ MPa$\sqrt{\text{m}}$ (Fünfschilling et al., 2010b), it results $-\sigma_{\text{mis}} \approx 350$–$500$ MPa. It should be noted that rather large T-stress values are necessary for the computed shift of the curves in Fig. 9(b). It has to be emphasized that the results obtained in this study can only give rough estimations due to the isotropic model used.

T-stresses in mechanical test specimens are mostly negligible. There are only a small number of tests exhibiting strongly negative T-stresses. Most important are the double cleavage drilled compression (DCDC) specimen (Fett et al., 2005b), the cone crack and, generally, notched specimens showing very small notch radii. It has been shown in Fett (2008), Fett and Munz (2006) that for slender notches in notched bending bars, as were used in Fett et al. (2008b), Fünfschilling et al. (2010b) for the R-curve determination, very strong compressive T-stresses occur. It can be concluded that during the first few micrometers of crack extension from a notch in a bending bar, maximum negative values of

$$\frac{T}{\sigma_{\text{bend}}} = -1.052\, F(a_0)\sqrt{\frac{a_0}{R}} \tag{17}$$

occur, where $F(a_0)$ is the geometric function for the stress intensity factor of a crack of depth a_0 and σ_{bend} is the outer fiber bending stress.

For the R-curve experiments on silicon nitride with Y_2O_3 and MgO content (Fünfschilling et al., 2010b), bending bars of $W = 4$ mm width were used with starter notches of $a_0 \approx 2.5$ mm depth having notch radii of $R = 6$–10 μm. The applied bending stresses were about 30–40 MPa. As can be seen from Fig. 10, only the first crack extensions of $\Delta a < 3$ μm are affected by the T-stress term. For these small crack extensions an effect on debonding must be expected.

From Fig. 10 it can be concluded that the T-stress after about $\Delta a = 1$ μm crack extension ($T/\sigma_{\text{bend}} \cong -18$) is on the order of $T \approx -650$ MPa. After 2 μm crack growth ($T/\sigma_{\text{bend}} \cong -8$), the T-stress drops to about $T \approx -280$ MPa. In terms of Fig. 9(b), this gives a shift of the critical kink angle from 57° to 51° and 54° for $T \approx -650$ MPa and $T \approx -280$ MPa, respectively.

Since debonding generally leads to a more compliant structure, the steepness of the R-curve is increased during the very first 2 μm crack extension. The effect on the $K_R(\Delta a)$-curves quickly becomes negligible for $\Delta a > 2$ μm.

Nevertheless, an effect on the bridging stresses must be expected for the special case of materials with steeply rising R-curves, such as with the present Si_3N_4 ceramic. It has been shown in Fünfschilling et al. (2010a) that the peak height of the bridging stresses in the crack-tip distance r is in a first-order approximation proportional to the steepness of the R-curve after a crack extension of $\Delta a = r$

$$\sigma_{\text{br}}\big|_{r=\Delta a} \propto -\frac{\mathrm{d}K_R}{\mathrm{d}a} \tag{18}$$

resulting in maximum stresses after about 2 μm crack extension, i.e., in the region of significant T-influence. As the consequence of the T-stress, the bridging stresses obtained within the notch influenced region are generally increased relative to the $T \approx 0$ condition. In this special steeply rising R-curve case, the peak bridging stress falls in the T-stress influenced region and a higher peak stress is seen relative to the C(T) specimen in Fig. 3(b).

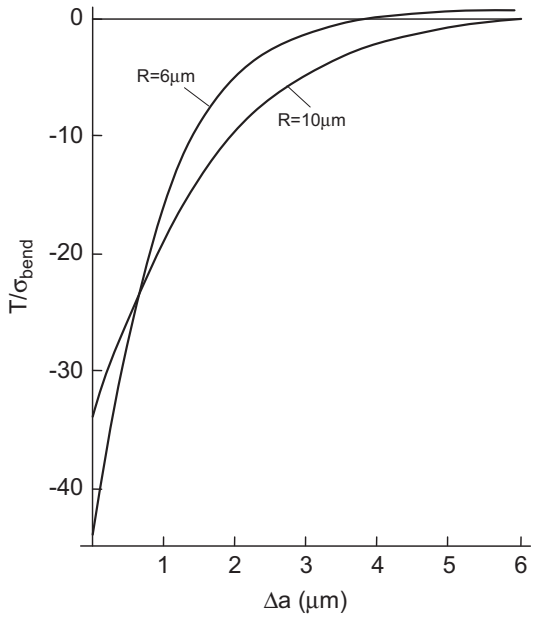

Fig. 10. *T*-stress for small cracks emanating from narrow notches in a bending bar according to (Fett, 2008).

As mentioned in Section 4.1 the C(T) bridging stresses are further reduced in Fig. 3(b) due to the free surface effects of the COD method. Accordingly, it is expected that the $T=0$ bridging stress distribution, which is expected to be a true material property, lies between the two curves in Fig. 3(b).

4.3. *Bridging stresses from spectroscopy methods*

As expected, the bridging stress distributions for the fatigue cracks had lower peak stresses than those measured with monotonically increasing loading due the cyclic bridging degradation. This is seen by comparing Figs. 3 and 6. Also, the general shapes of the Raman measured bridging stress distributions appear reasonable and in agreement with the other methods. The measured location of the stress peak is also similar from specimen to specimen indicating a low degree of scatter in the distribution shape.

However, difficulties were encountered in measuring the magnitudes of the bridging stress profiles for silicon nitride using Raman spectroscopy. The peak bridging stresses from Raman spectroscopy demonstrate significant scatter and also a dependence on specimen color (Fig. 4(b)). The scatter tends to be more pronounced in the darker samples (Fig. 4(b)). Furthermore, the average peak stress for the light grey colored samples was only ~36% that of the black samples (Fig. 6).

The increased scatter can be explained by the 50% increase of sampling depth and almost doubling of the sampling volume from the dark to light specimens (Fig. 7). When using a microprobe to measure bridging stresses it is important to recognize that bridges are discrete entities with variable individual bridging forces. Based on Fig. 7 nearly twice as many bridging grains were sampled in the light grey specimens as compared to the dark specimens. Sampling more grains per measurement allows for (1) more averaging of bridges carrying various loads and (2) more averaging of grains located between the bridges that bear zero load. With the smaller sampling volume the fluctuations in measurements will be exaggerated depending on the number of high, low, and zero load bearing grains measured. Doubling the sampling volume decreases this sampling error by averaging over more grains and better approximating the through thickness average. Thus, less scatter is observed with the light grey samples.

Additionally, the higher average peak stress measured for the dark samples (Fig. 6) can be rationalized by the fact that the microprobe sampling is confined to grains at or near to the surface. Here it is important to note that near surface bridges will be more compliant than subsurface bridges as described in Section 4.1, thus giving a larger amount of strain at a given stress level. Furthermore, grains deeper inside the materials are confined on all sides by surrounding grains and will experience less strain at a given stress. The Raman spectroscopy technique is basically a measurement of lattice strain which is then converted to stress by a calibration factor. Accordingly, the less constrained surface bridges will be expected to give an relatively high stress estimate based on the Raman shift. With a larger sampling volume more subsurface bridges are averaged with the surface bridges to give a value closer to the through thickness average for the light grey samples.

In contrast to the Si_3N_4 Raman results, it has been reported that the fluorescence spectroscopy method gives accurate agreement with the *R*-curve method for determining the bridging stress distribution of fatigue cracks in C(T) samples (Fig. 2). As mentioned above, the *R*-curve method has the advantage of giving a through thickness average that is not significantly biased by the surface condition. Additionally, in Gallops et al. (2011a) the *R*-curve was measured only with cracks outside of the influence of the notch, so *T*-stress effects were negligible. The excellent agreement with the

fluorescence results is explained by the fact that ~2.5% of the sample thickness was sampled by the fluorescence microprobe due to the translucent optical properties of Al_2O_3. Accordingly, ample material was sampled to obtain an average distribution that roughly represents the through thickness average and agrees with the *R*-curve result. Accordingly, it is concluded that in the absence of *T*-stresses a bridging distribution can be determined that is a true material property. Furthermore, it can be independently measured by different techniques provided adequate through thickness sampling is utilized in the method. In the alumina case 2.5% of the thickness appears adequate.

4.4. Deducing the fatigue bridging stress distribution

The Si_3N_4 material used in the study represents a special class of materials where the *R*-curves rise very quickly over the first few micrometers of crack growth. This requires very specialized techniques to measure the fracture *R*-curve, $K_R(\Delta a)$, as described in Fünfschilling et al. (2009b), Fünfschilling et al. (2010b). In fatigue it is essentially impossible to control fatigue crack propagation at these size scales. Thus, the direct measurement of the fatigue threshold *R*-curve as described in Gallops et al. (2011a), Gallops et al. (2011b), Pippan et al. (2001) is practically impossible. Nevertheless, understanding and predicting the fatigue failure behavior of these materials has technological importance (Danzer and Lengauer, 2010; Harrer et al., 2011) and knowledge the bridging stress distribution for a fatigue crack can enable the calculation of the fatigue threshold *R*-curve via Eqs. (1)–(3). The fatigue threshold *R*-curve can then be used to predict fatigue behavior as demonstrated in Gallops et al. (2011a).

In this regard, a new method for deducing a best estimate bridging stress distribution for a fatigue crack has been presented (Fig. 5). By using the best estimate of the distribution shape from the fracture *R*-curve and degrading the peak magnitude to match the measured fatigue behavior this method should be insensitive to many of the problems described above. Indeed, the problems described above focus largely on errors in the bridging stress peak magnitude, and in Fig. 5 the peak magnitude was independently determined from fatigue threshold experiments using Eqs. (1)–(3). Future work will focus on verifying the accuracy of fatigue predictions based on the deduced bridging distribution (Fig. 5) as has been done for Al_2O_3 in Gallops et al. (2011a).

Alternatively one could attempt to improve the spectroscopy results by increasing the sampling volume similar to alumina; however, this is dependent on the optical properties of the material which is usually not a controllable variable. Another approach could be to increase the number of specimens sampled. Based on the results in Fig. 6 it may be suspected that with enough samples a reliable average might be attained; however, with such limited sampling volume some biasing of the surface stress state would always be retained making this alternative less attractive. Also, this approach would require more experimental time and material to be used. While increasing the laser power may be a way to decrease the data collection time, sample heating will occur giving unreliable Raman results. Furthermore, increasing the laser power will not increase the sampling volume as that is dependent solely on the absorption coefficient of the material. Overall, while it was instructive to use the Raman technique to verify the approximate bridging distribution shape, it does not appear to be reliable and/or time efficient as a stand-alone technique for determining the bridging stress distribution in the present Si_3N_4 where the sampling volume was severely limited to only 0.1–0.2% of the sample thickness. It is expected that Raman spectroscopy would be more useful when better penetration depth is achieved.

5. Conclusions

Based on a comparison of bridging stresses measured for grain bridging ceramics using *R*-curve, COD, and spectroscopy methods, the following conclusions may be made:

- The COD method is surface sensitive and gives a lower peak bridging stress for Si_3N_4 compared to the *R*-curve technique which samples through the entire material thickness. This effect is caused by reduced compressive residual stresses normal to the crystal length axis that affect the critical crack terminating angle Θ_{cr} and give increased debonding lengths ℓ. Grains acting as frictional bridges also undergo reduced friction stresses. These factors give a more compliant near surface bridging zone and lower the calculated bridging stress.
- When *R*-curves rise steeply over the first few micrometers of growth from a notch, as is common for Si_3N_4 and some other ceramics, an effect of negative *T*-stress is expected to raise the *R*-curve determined peak bridging stress. This effect is attributed to a reduction in the critical angle Θ_{cr} for grain debonding and the concurrent steepening of the *R*-curve.
- Comparing the results for Al_2O_3 and Si_3N_4, it is concluded that spectroscopy methods only yield reliable bridging stress results if a reasonable through thickness volume of material is sampled. While 2.5% of the specimen thickness achieved using fluorescence spectroscopy appears adequate for Al_2O_3, the 0.1–0.2% of the sample thickness achieved using Raman spectroscopy for Si_3N_4 appears inadequate.
- Another conclusion based on a comparison of Al_2O_3 and Si_3N_4 data is that in the absence of *T*-stresses a bridging distribution $\sigma_{br}=f(\delta)$ can be determined that is a true material property. Furthermore, it can be independently measured by different techniques provided adequate through thickness sampling is utilized in the method. In the alumina case 2.5% of the thickness appears adequate.

- A new method has been proposed for determining the bridging stresses of fatigue cracks for materials where *R*-curves rise steeply over the first few micrometers of growth from a notch, as is common for Si_3N_4 and some other ceramics. In this new method the fatigue crack bridging stress distribution is deduced from (1) the bridging stress distribution for monotonically loaded cracks and (2) experimental fatigue data.

Acknowledgements

J.J. Kruzic, R.B. Greene, and S. Gallops would like to acknowledge support from the National Science Foundation CAREER Award No. 0547394. S. Fünfschilling and M.J. Hoffmann would like to thank the Deutsche Forschungsgemeinschaft DFG for financing parts of this work within the SFB 483. Finally, the authors would also like the thank Dr. Raphaelle Satet for help with the COD experiments, Ram Ravichandran with assistance in measuring the optical absorption coefficients, and Dr. Ho-Kyung Kim of Seoul National University of Technology for providing the in-situ loading stage used for the spectroscopy experiments.

References

ASTM, 2010. ASTM E647–08 — Standard Test Method for Measurement of Fatigue Crack Growth Rates, Annual Book of ASTM Standards, Vol. 03.01: Metals-Mechanical Testing; Elevated and Low-temperature Tests; Metallography. ASTM International, West Conshohocken, Pennsylvania, USA, http://dx.doi.org/10.1520/E0647-1508E1501.

Becher, P.F., 1991. Microstructural design of toughened ceramics. J. Am. Ceram. Soc. 74, 255–269.

Belnap, J.D., Shetty, D.K., 1998. Micromechanics of crack bridging in sapphire epoxy composites. Compos. Sci. Technol. 58, 1763–1773.

Belnap, J.D., Shetty, D.K., 2005. Interfacial properties of sapphire/epoxy composites: comparison of fluorescence spectroscopy and fiber push-in techniques. Compos. Sci. Technol. 65, 1851–1860.

Bennett, J.A., Young, R.J., 2008. A strength based criterion for the prediction of stable fibre crack-bridging. Compos. Sci. Technol. 68, 1282–1296.

Bennison, S.J., Lawn, B.R., 1989. Role of interfacial grain-bridging sliding friction in the crack-resistance and strength properties of nontransforming ceramics. Acta Metall. 37, 2659–2671.

Bloyer, D.R., Venkateswara Rao, K.T., Ritchie, R.O., 1998. Fracture toughness and *R*-curve behavior of laminated brittle-matrix composites. Metall. Mater. Trans. 29A, 2483–2496.

Buchanan, D.J., John, R., Johnson, D.A., 1997. Determination of crack bridging stresses from crack opening displacement profiles. Int. J. Fract. 87, 101–117.

Campbell, J.P., Venkateswara Rao, K.T., Ritchie, R.O., 1999. The effect of microstructure on fracture toughness and fatigue-crack growth behavior in γ-based titanium aluminide intermetallics. Metall. Mater. Trans. 30A, 563–577.

Cox, B.N., Marshall, D.B., 1991. The determination of crack bridging forces. Int. J. Fract. 49, 159–176.

Danzer, R., Lengauer, M., 2010. Silicon nitride materials for hot working of high strength metal wires. Eng. Fail. Anal. 17, 596–606.

Dassios, K.G., Galiotis, C., Kostopoujos, V., Steen, M., 2003. Direct in situ measurements of bridging stresses in CFCCs. Acta Mater. 51, 5359–5373.

Dauskardt, R.H., Ager, J.W., 1996. Quantitative stress mapping in alumina composites by optical fluorescence imaging. Acta Mater. 44, 625–641.

Deans, W.F., Richards, C.E., 1979. A simple and sensitive method of monitoring crack and load in compact fracture mechanics specimens using strain gages. J. Test. Eval. 7, 147–154.

Dowling, N.E., 1979. Notched member fatigue life predictions combining crack initiation and propagation. Fatigue Eng. Mater. Struct. 2, 129–138.

Fett, T., 1995a. Determination of bridging stresses and *R*-curves from load-displacement curves. Eng. Fract. Mech. 52, 803–810.

Fett, T., 1995b. Evaluation of the bridging relation from crack-opening-displacement measurements by use of the weight function. J. Am. Ceram. Soc. 78, 945–948.

Fett, T., 2008. Stress Intensity Factors, *T*-Stresses, Weight Functions. Universitätsverlag Karlsruhe, Karlsruhe.

Fett, T., Funfschilling, S., Hoffmann, M.J., Oberacker, R., 2008a. Different *R*-curves for two- and three-dimensional cracks. Int. J. Fract. 153, 153–159.

Fett, T., Fünfschilling, S., Hoffmann, M.J., Oberacker, R., Jelitto, H., Schneider, G.A., 2008b. *R*-curve determination for the initial stage of crack extension in Si_3N_4. J. Am. Ceram. Soc. 91, 3638–3642.

Fett, T., Munz, D., 1997. Stress Intensity Factors and Weight Functions. Computational Mechanics Publications, Southampton, UK.

Fett, T., Munz, D., 2006. Influence of narrow starter notches on the initial crack growth resistance curve of ceramics. Arch. Appl. Mech. 76, 667–679.

Fett, T., Munz, D., Geraghty, R.D., White, K.W., 2000. Bridging stress determination by evaluation of the *R*-curve. J. Eur. Ceram. Soc. 20, 2143–2148.

Fett, T., Munz, D., Nijwa, A.B.K., Rödel, J., Quinn, G.D., 2005a. Bridging stresses in sintered reaction-bonded Si3N4 from COD measurements. J. Eur. Ceram. Soc. 25, 29–36.

Fett, T., Munz, D., Thun, G., Bahr, H.-A., 1995. Evaluation of bridging parameters in alumina from *R*-curves by use of the fracture mechanical weight function. J. Am. Ceram. Soc. 78, 949–951.

Fett, T., Rizzi, G., Munz, D., 2005b. T-stress solution for DCDC specimens. Eng. Fract. Mech. 72, 145–149.

Foote, R.M.L., Mai, Y.W., Cotterell, B., 1986. Crack-growth resistance curves in strain-softening materials. J. Mech. Phys. Solids 34, 593–607.

Fünfschilling, S., Fett, T., Gallops, S.E., Kruzic, J.J., Oberacker, R., Hoffmann, M.J., 2010a. First- and second-order approaches for the direct determination of bridging stresses from *R*-curves. J. Eur. Ceram. Soc. 30, 1229–1236.

Fünfschilling, S., Fett, T., Hoffmann, M., Oberacker, R., Jelitto, H., Schneider, G., 2009a. Determination of the crack-tip toughness in silicon nitride ceramics. J. Mater. Sci. 44, 335–338.

Fünfschilling, S., Fett, T., Hoffmann, M.J., Oberacker, R., Jelitto, H., Schneider, G.A., Härtelt, M., Riesch-Oppermann, H., 2009b. Bridging stresses from *R*-curves of silicon nitrides. J. Mater. Sci. 44, 3900–3904.

Fünfschilling, S., Fett, T., Hoffmann, M.J., Oberacker, R., Schwind, T., Wippler, J., Böhlke, T., Özcoban, H., Schneider, G.A., Becher, P.F., Kruzic, J.J., 2011. Mechanisms of toughening in silicon nitrides: roles of crack bridging and microstructure. Acta Mater. 59, 3978–3989.

Fünfschilling, S., Fett, T., Oberacker, R., Hoffmann, M.J., Özcoban, H., Jelitto, H., Schneider, G.A., Kruzic, J.J., 2010b. *R*-curves from compliance and optical crack-length measurements. J. Am. Ceram. Soc. 93, 2814–2821.

Gallops, S., Fett, T., Ager III, J.W., Kruzic, J.J., 2011a. Fatigue threshold *R*-curves predict small crack fatigue behavior of bridging toughened materials. Acta Mater. 59, 7654–7661.

Gallops, S., Fett, T., Kruzic, J.J., 2011b. Fatigue threshold *R*-curve behavior of grain bridging ceramics: role of grain size and grain boundary adhesion. J. Am. Ceram. Soc. 94, 2556–2561.

Geraghty, R.D., Hay, J.C., White, K.W., 1999. Fatigue degradation of the crack wake zone in monolithic alumina. Acta Mater. 47, 1345–1353.

Gilbert, C.J., Ritchie, R.O., 1998. On the quantification of bridging tractions during subcritical crack growth under monotonic and cyclic fatigue loading in a grain-bridging silicon carbide ceramic. Acta Mater. 46, 609–616.

Harrer, W., Morrell, R., Lengauer, M., Danzer, R., Berroth, K., Zleppnig, W., 2011. Failure analysis of silicon nitride rings for hot rolling of highly alloyed steel and superalloy wires. Eng. Fail. Anal. 18, 138–147.

Hay, J.C., White, K.W., 1993. Grain-bridging mechanisms in monolithic alumina and spinel. J. Am. Ceram. Soc. 76, 1849–1854.
He, J., Clarke, D.R., 1995. Determination of the piezospectroscopic coefficients for chromium-doped sapphire. J. Am. Ceram. Soc. 78, 1347–1353.
Hu, X.Z., Lutz, E.H., Swain, M.V., 1991. Crack-tip-bridging stresses in ceramic materials. J. Am. Ceram. Soc. 74, 1828–1832.
Hu, X.Z., Mai, Y.W., 1992. Crack-bridging analysis for alumina ceramics under monotonic and cyclic loading. J. Am. Ceram. Soc. 75, 848–853.
Kruzic, J.J., Cannon, R.M., Ager III, J.W., Ritchie, R.O., 2005a. Fatigue threshold *R*-curves for predicting reliability of ceramics under cyclic loading. Acta Mater. 53, 2595–2605.
Kruzic, J.J., Cannon, R.M., Ritchie, R.O., 2004. Crack-size effects on cyclic and monotonic crack growth in polycrystalline alumina: quantification of the role of grain bridging. J. Am. Ceram. Soc. 87, 93–103.
Kruzic, J.J., Nalla, R.K., Kinney, J.H., Ritchie, R.O., 2003. Crack blunting, crack bridging and resistance-curve fracture mechanics in dentin: effect of hydration. Biomaterials 24, 5209–5221.
Kruzic, J.J., Satet, R., Hoffmann, M.J., Cannon, R.M., Ritchie, R.O., 2008. The utility of *R*-curves for understanding fracture toughness-strength relations in bridging ceramics. J. Am. Ceram. Soc. 91, 1986–1994.
Kruzic, J.J., Schneibel, J.H., Ritchie, R.O., 2005b. Ambient- to elevated-temperature fracture and fatigue properties of Mo–Si–B alloys: role of microstructure. Metall. Mater. Trans. 36A, 2393–2402.
Mai, Y.-W., Lawn, B.R., 1987. Crack-interface grain bridging as a fracture resistance mechanism in ceramics: II, Theoretical fracture mechanics model. J. Am. Ceram. Soc. 70, 289–294.
Marshall, D.B., Cox, B.N., Evans, A.G., 1985. The mechanics of matrix cracking in brittle-matrix fiber composites. Acta Metall. 33, 2013–2021.
Nairn, J.A., Liu, S.L., Chen, H.H., Wedgewood, A.R., 1991. Longitudinal splitting in epoxy and *K*-polymer composites — Shear lag analysis including the effect of fiber bridging. J. Compos. Mater. 25, 1086–1107.
Nalla, R.K., Kruzic, J.J., Kinney, J.H., Ritchie, R.O., 2005. Mechanistic aspects of fracture and *R*-curve behavior of human cortical bone. Biomaterials 26, 217–231.
Palazotto, A.N., Mercer, J.G., 1990. Crack considerations in a notched compact tension specimen. Eng. Fract. Mech. 37, 473–492.
Pezzotti, G., 1999. In situ study of fracture mechanisms in advanced ceramics using fluorescence and Raman microprobe spectroscopy. J. Raman Spectrosc. 30, 867–875.
Pezzotti, G., Ichimaru, H., Ferroni, L.P., Hirao, K., Sbaizero, O., 2001. Raman microprobe evaluation of bridging stresses in highly anisotropic silicon nitride. J. Am. Ceram. Soc. 84, 1785–1790.
Pezzotti, G., Muraki, N., Maeda, N., Satou, K., Nishida, T., 1999a. In situ measurement of bridging stresses in toughened silicon nitride using Raman microprobe spectroscopy. J. Am. Ceram. Soc. 82, 1249–1256.
Pezzotti, G., Okuda, H., Muraki, N., Nishida, T., 1999b. In-situ determination of bridging stresses in Al_2O_3/Al_2O_3-platelet composites by fluorescence spectroscopy. J. Eur. Ceram. Soc. 19, 601–608.
Pezzotti, G., Sakakura, S., 2003. Study of the toughening mechanisms in bone and biomimetic hydroxyapatite materials using Raman microprobe spectroscopy. J. Biomed. Mater. Res. 65A, 229–236.
Pezzotti, G., Sbaizero, O., Sergo, V., Muraki, N., Maruyama, K., Nishida, T., 1998. In situ measurements of frictional bridging stresses in alumina using fluorescence spectroscopy. J. Am. Ceram. Soc. 81, 187–192.
Pezzotti, G., Suenobu, H., Nishida, T., Sbaizero, O., 1999c. Measurement of microscopic bridging stresses in an alumina molybdenum composite by in situ fluorescence spectroscopy. J. Am. Ceram. Soc. 82, 1257–1262.
Pippan, R., Hageneder, P., Knabl, W., Clemens, H., Hebesberger, T., Tabernig, B., 2001. Fatigue threshold and crack propagation in γ-TiAl sheets. Intermetallics 9, 89–96.
Preuss, M., Rauchs, G., Doel, T.J.A., Steuwer, A., Bowen, P., Withers, P.J., 2003. Measurements of fibre bridging during fatigue crack growth in Ti/SiC fibre metal matrix composites. Acta Mater. 51, 1045–1057.
Raddatz, O., Schneider, G.A., Claussen, N., 1998. Modelling of *R*-curve behaviour in ceramic/metal composites. Acta Mater. 46, 6381–6395.
Satet, R.L., Hoffmann, M.J., 2005. Influence of the rare-earth element on the mechanical properties of RE–Mg bearing silicon nitride. J. Am. Ceram. Soc. 88, 2485–2490.
Sorensen, L., Botsis, J., Gmur, T., Humbert, L., 2008. Bridging tractions in mode I delamination: measurements and simulations. Compos. Sci. Technol. 68, 2350–2358.
Sternberg, S.R., 1983. Biomedical image processing. Computer 16, 22–34.
Studer, M., Peters, K., Botsis, J., 2003. Method for determination of crack bridging parameters using long optical fiber Bragg grating sensors. Composites Part B 34, 347–359.
Walls, D.P., Zok, F.W., 1994. Interfacial fatigue in a fiber-reinforced metal–matrix composite. Acta Metall. Mater. 42, 2675–2681.
White, K.W., Hay, J.C., 1994. Effect of thermoelastic anisotropy on the *R*-curve behavior of monolithic alumina. J. Am. Ceram. Soc. 77, 2283–2288.